Research article

Victor Pacheco-Peña, Rúben A. Alves and Miguel Navarro-Cía*

From symmetric to asymmetric bowtie nanoantennas: electrostatic conformal mapping perspective

https://doi.org/10.1515/nanoph-2019-0488
Received November 29, 2019; revised January 8, 2020; accepted January 9, 2020

Abstract: Plasmonic nanoantennas have revolutionized the way we study and modulate light–matter interaction. Due to nanofabrication limitations, dimer-type nanoantennas always exhibit some degree of asymmetry, which is desirable in some cases. For instance, in sensing applications, asymmetry is sometimes induced by design in plasmonic nanoantennas to favor higher order nonradiative modes with sharp Fano line shapes. Regardless of the actual origin of the asymmetry, unintentional or intentional, an analytical frame that can deal with it in a seamless manner would be beneficial. We resort to conformal mapping for this task and we track the influence of the degree of asymmetry of the circular sectors composing gold bowtie nanoantennas on the nonradiative Purcell enhancement of a nearby nanoemitter. This manuscript reviews the contributions of conformal mapping to plasmonic nanoantennas and illustrates the advantages of the elegant analytical solution provided by conformal mapping to grasp physical insights, which can serve as a springboard for new plasmonic asymmetric nanoantenna designs.

Keywords: conformal mapping; nanoantennas; plasmonics.

PACS: 41.20.Cv; 73.20.Mf; 78.67.Bf; 78.90.+t.

***Corresponding author: Miguel Navarro-Cía,** School of Physics and Astronomy, University of Birmingham, Birmingham B15 2TT, United Kingdom, e-mail: m.navarro-cia@bham.ac.uk.
https://orcid.org/0000-0003-0256-6465
Victor Pacheco-Peña: School of Engineering, Newcastle University, Merz Court, Newcastle Upon Tyne NE1 7RU, United Kingdom.
https://orcid.org/0000-0003-2373-7796
Rúben A. Alves: School of Physics and Astronomy, University of Birmingham, Birmingham B15 2TT, United Kingdom.
https://orcid.org/0000-0001-7916-1402

1 Introduction

Nanoantennas and nanocavities supporting plasmonic modes (collective oscillation of conduction electrons induced by an electromagnetic wave) with extraordinary small mode volumes are ideal systems for studying light–matter interaction and provide a natural platform for sensing and trapping [1]. Some of the latest achievements in the field include single-molecule fluorescence [2] and strong-coupling at room temperature [3], effective third-order susceptibility of 3.5×10^3 nm^2/V^2 [4], second harmonic generation conversion efficiency of 0.075% [5], probing vibrations of individual molecular bonds [6] and the nonlocal response of the graphene electron liquid [7], spontaneous emissions that are faster than stimulated emission [8], ultrafast modulation in a single metal layer [9] and low-loss plasmon-assisted electro-optic modulation [10], among others.

The current standard for designing such nanostructures are time-consuming computational tools whose limitations are not always understood by the user. In many cases, such simulations do not provide a physical understanding or intuition of the scenario that could be exploited for future nanosystems. In fact, such physical intuition is highly regarded to unveil hidden symmetries [11–13] and understand the consequences of inducing asymmetries in the electrodynamic response of plasmonic nanostructures [14–17]. This problem can be alleviated by using analytical tools, such as transformation optics [18, 19] or its two-dimensional (2D) variant, conformal transformation [19, 20], which we have exploited over the last few years [13, 21–27].

Conformal mapping is an important technique used in complex analysis, which enables solving many boundary problems found in physics and engineering disciplines. The most classical example of conformal mapping beyond pure mathematics is, perhaps, the first successful airfoil theory developed by Joukowski/Zhukovsky at the beginning of the 20th century [28]. In the field of electromagnetics, this analytical tool has

been used extensively to analyze the transmission lines found nowadays in radio-frequency and microwave integrated circuits [29]. Its application for plasmonics nanoantennas has been championed just recently by Pendry et al. [19, 30–34], who have also extended it to graphene gratings [12, 35]. Other contributors to the field of transformation optics nanoantennas include Werner et al. [36], Zayats et al. [37, 38] and ourselves [13, 21–27]. While other groups have dealt with cylindrical [30–32, 36, 39–41] and spherical dimers [42, 43], crescent-shaped nanostructures [30, 36, 44, 45], cylindrical nanocavities and nanoprotrusion [33, 34], nanoparticle-on-a-mirror [42] and core-shell nanoparticles [37, 38], our efforts have been devoted instead to understand the interaction of a quantum emitter nearby bowtie nanostructures [13, 25–27] and the prospect of bowtie-modified nanostructures (i.e. logperiodic nanoantennas) for higher harmonic generation [21, 22] and spectroscopy [23, 24]. The motivation to work with such topology stems from the fact that the plasmonic community holds it in high regard given its broadband response and high field concentration at the gap [2, 46–49].

In this manuscript, we review the conformal mapping that enables us to transpose the complicated bowtie scenario to the simpler periodic metal-insulator scenario (Figure 1). We also report new results to address the following questions: (1) does the surface plasmon reflection phase have any asymptotic limit with the nanoantenna size? and (2) what is the effect of asymmetric circular sectors on the overall response of the bowtie excited by a nearby nanoemitter?

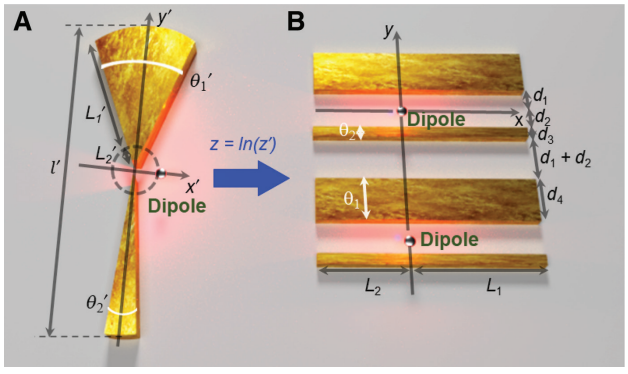

Figure 1: Transformed and original space for the nanoantennas under study.
The schematic representation of the gold asymmetric bowtie nanoantenna (A) along with its corresponding transformed periodic metal-insulator geometry (B) after applying the conformal mapping shown in the figure in blue. The total length of the bowtie $l' = 2(L_{1'} + L_{2'}) + g'$, where g' is the size of the gap. $g' = 1$ nm unless otherwise stated and the nanoemitter is located at $(x', y') = (1\text{ nm}, 0\text{ nm})$. Notice that both structures are invariant along z' and z for the analytical results of this manuscript.

2 Analytical framework, results and discussion

2.1 Conformal mapping: basics

A conformal map is an analytic transformation of the form $z' = f(z)$, where $z' = x' + iy'$, which preserves oriented angles locally. Hence, the tangential component of the electric field $E_{\parallel}$ and the normal component of the displacement field, $D_{\perp}$ are conserved under the transformation, implying that the material in the original and transformed spaces are identical. That is,

$$\varepsilon'(z') = \varepsilon(f^{-1}(z')) = \varepsilon(z). \tag{1}$$

Furthermore, if a given function $\Phi(z)$ is a solution of Laplace's equation for the z-plane, representing the quasi-static potential in such plane, then $\Phi'(z') = \Phi(f^{-1}(z'))$ (the quasi-static potential in z'-plane) will be the Laplace solution for the z'-plane.

Let us now imagine that the geometry under study is a 2D bowtie geometry [i.e. a three-dimensional (3D) bowtie geometry with out-of-plane invariance] with a nanoemitter at $(x', y') = (1\text{ nm}, 0\text{ nm})$ modelled as a line dipole (Figure 1A). By using the natural logarithm mapping

$$z = ln(z'), \tag{2}$$

such geometry is transformed into the periodic metal-insulator geometry shown in Figure 1B. In particular, the nanoemitter at $(x', y') = (1\text{ nm}, 0\text{ nm})$ is transposed to $(x, y) = (0, 2\pi m)$, where m is an integer. If the nanoemitter were on-center in the original frame, it would be transposed to $x = -\infty$. The fact that the bowtie has a gap at its center prevents the metal-insulator geometry to extend to $-\infty$ in the x-direction.

If we restrict the bowtie to be at least one order of magnitude smaller than the wavelength, we can invoke the quasi-static approximation for the analytical analysis, whereby the radiation losses are neglected and the magnetic and electric fields are decoupled; the latter field can then be expressed via an electrostatic potential satisfying the Laplace equation. In this situation, the power dissipations in the original, $P_{\text{abs}}^{(x',y')}$, and transformed, $P_{\text{abs}}^{(x,y)}$, frames are identical. Hence, the former can be calculated using the latter, whereby the electric field is evaluated at the dipole position as

$$P_{nr} = -(1/2)\omega\Im[p_x^* E_{1x}^S(0,\ 2\pi m) + p_y^* E_{1y}^S(0,\ 2\pi m)], \quad (3)$$

where P_{nr} is the nonradiative power emission; ω is the angular frequency; p_x and p_y are the x and y components of the dipole moment with magnitude $|p|$, respectively; and $E_{1x}^S(0,\ 2\pi m)$ and $E_{1y}^S(0,\ 2\pi m)$ are the x and y components of the electric field, respectively, at the position where the dipole is in the transformed frame. Normalizing P_{nr} to the power radiated by the line (2D) dipole

$$P_0 = -(1/16)\omega^3 \mu_0 |p|^2, \quad (4)$$

where μ_0 is the permeability in the free space, results in the nonradiative Purcell enhancement given by

$$\overline{\Gamma_{nr}} = P_{nr}/P_0, \quad (5)$$

provided an intrinsic quantum yield of 1 is used for the nanoemitter; under such condition, one can map the nonradiative decay experienced by the nanoemitter with the power absorbed by the bowtie nanoantenna [50].

Such nonradiative Purcell enhancement is modulated by the coupling between the array of line dipoles and the plasmonic eigen-modes of the system [notice the explicit field overlap in Eq. (3)] since the latter modes are the only effective nonradiative channels of the system. These plasmonic eigen-modes are nothing but the localised surface plasmons resulting from the interference of the surface plasmons triggered by line dipoles. These are reflected back and forth between the two ends of the periodic metal-insulator geometry (i.e. standing-wave plasmonic resonances) and have a wavenumber $k = (n\pi - \Delta\varphi)/(L_1 + L_2)$, with $n = 1, 2, 3, \ldots$, and $L_1 + L_2$ representing the order of the standing-wave plasmonic resonance and the total length of the periodic metal-insulator cavities, respectively, and $\Delta\varphi$ is a reflection phase correction. This will be discussed in the following subsection. The reader is referred to Figure 1 to see the definition of geometrical parameters. The complete mathematical derivation describing this underlying mechanism can be found in Section 3.

2.2 Surface plasmon reflection phase

The surfaces plasmons acquire a nontrivial phase at both ends of the periodic metal-insulator geometry associated with the near-field energy storage at these end faces. This is included in our model through a semi-empirical phase correction $\Delta\varphi$, which is added to the reflection phase of an open boundary (i.e. π) [25]. An analytical solution to the surface plasmon reflection phase could be attempted, but only under some assumptions, such as ignoring the evanescent plasmonic modes [51, 52]. This approximation is valid for long enough periodic metal-insulator cavities (i.e. large enough bowtie), and results into an asymptotic value of the surface plasmon reflection phase at long wavelengths where metal has a large negative dielectric constant. However, for short periodic metal-insulator cavities, and thus, small bowties as those considered in our

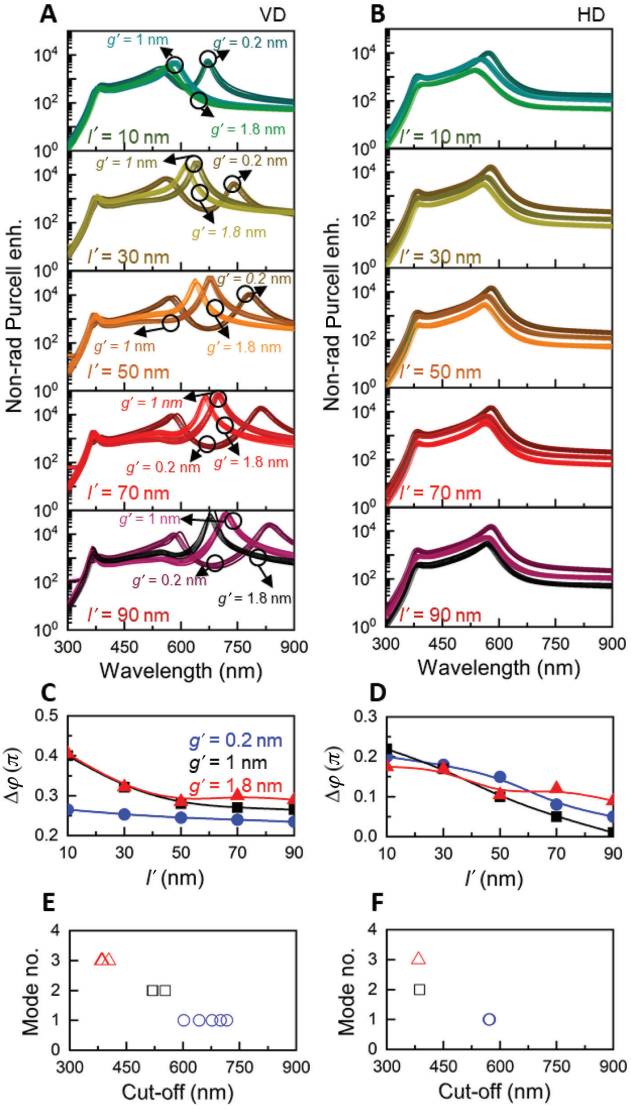

Figure 2: Influence of the bowtie nanoantenna's length (l'). The analytical (symbols) and numerical (solid lines) results of the $\overline{\Gamma_{nr}}$ for $\theta' = 20°$ bowtie nanoantenna of varying length l' and gap size g' illuminated by a nanoemitter with vertical (A) and horizontal (B) polarizations placed at $(x', y') = (1\text{ nm}, 0\text{ nm})$. Notice that the symbols and solid lines overlap and are largely indistinguishable. Phase correction $\Delta\varphi$ as a function of l' for the vertical (C) and horizontal nanoemitters (D) for the three gap sizes considered in A and B. The cut-off wavelength for the first three localized surface plasmon modes with a vertical (E) and horizontal nanoemitter (F) when $g' = 1$ nm. Notice that the cut-off wavelength for all modes is rather stable against g' for the horizontal nanoemitter case.

electrostatic conformal mapping works, this approximation is not valid.

Figure 2 plots $\overline{\Gamma_{nr}}$ along with the corresponding phase correction $\Delta\varphi$ for $\theta' = 20°$ bowtie nanoantennas of varying size $l' = 2(L'_1 + L'_2) + g'$ (see definition of geometrical parameters in Figure 1) and gap size g' where the nanoemitter is vertical or horizontal. For the horizontal case, all plasmonic eigen-modes emerge at a similar wavelength regardless of l' and g'. Specifically, the wavelength of the fundamental mode is around 575 nm, whereas higher order plasmonics modes are agglomerated close to the surface plasmon wavelength. This is confirmed by plotting the cut-off wavelength of the first three eigen-modes (i.e. computed via the divergence of the coefficient of the scattered potential in the region where the dipole is present, $B_{\pm}$, see Figure 2F). The vertical case shows a completely different picture. The fundamental plasmonic eigen-mode dramatically red-shifts significantly with l' (see Figure 2A and E) with decreasing g' for a fixed l' (Figure 2A). In addition, the first higher order eigen-mode is not agglomerated close to the surface plasmon wavelength as the rest of higher order modes, but it appears around 525 nm.

From Figure 2C and D, one can observe how the phase correction tends rapidly to an asymptotic value as the size of the bowtie (i.e. length of the periodic metal-insulator cavities) increases for a vertical nanoemitter (panel C), whereas the phase correction undergoes a larger excursion and drops more monotonically down to 0 rad for a horizontal nanoemitter (panel D). This polarization-dependent response can be understood from the transmission line representation of the classical Sommerfeld half-space problem [53, 54] and based on the strong influence of evanescent plasmonic modes in the surface plasmon reflection phase [51]. A vertical Hertzian dipole contributes a voltage source on a transverse-magnetic (TM) transmission line analog, whereas a horizontal dipole contributes current sources on both the TM and transverse-electric (TE) transmission lines [53]. As such, the latter deals with a larger number of evanescent plasmonic modes that can only be neglected for a larger bowties than for vertical dipoles. The fact that $\Delta\varphi$ for $g' = 0.2$ nm and a vertical nanoemitter is rather flat compared to the other gap sizes is due to the diminishing influence of the evanescent plasmonic modes in the corresponding long metal-insulator cavity.

2.3 Asymmetric nanoantennas

Manufactured nanoantennas suffer from inevitable imperfections due to the nanofabrication process. Bowtie nanoantennas are not free of such issues. Thus, it would be useful to understand the impact of these imperfections in the response of bowtie nanoantennas. The analytical frame described here cannot describe precisely all types of imperfections, but it can at least assist with simple deformations, such as asymmetries between the monomers composing the dimer. We study in this section the effect of asymmetric circular sectors comprising the bowtie nanoantennas. A general illustration of this nanoantenna is shown in Figure 1A, where the angles of the two arms (made of gold) are different $\theta'_1 \neq \theta'_2$. Notice that without loss of generality, the nanoemitter remains at $(x', y') = (1\text{ nm}, 0\text{ nm})$ in the original frame.

With this configuration, let us first consider the asymmetric $l' = 20$ nm and $g' = 1$ nm bowtie nanoantennas with $\theta'_1 = 20°$ and varying θ'_2. The schematic representations, including dipole position and polarization, are shown in Figure 3A and B above their corresponding results. The results of the nonradiative Purcell enhancement $\left(\overline{\Gamma_{nr}}\right)$ spectra as a function of θ'_2 ranging from 10° to 40° are shown in Figure 3E and F considering a vertical and horizontal polarization of the nanoemitter, respectively. The main observation from these results is that the localized surface plasmon modes are blue-shifted when changing θ'_2. This performance is in agreement with our previous works considering symmetric bowtie and tripod nanoantennas and nanocavities [13, 25–27]. However, there is an interesting difference: the blue-shift is smaller for the asymmetric nanoantennas compared to the symmetric ones. For instance, for the vertical nanoemitter shown in Figure 3A, the localized surface plasmon mode of order $n = 1$ is blue-shifted from $\lambda = 697$ nm to $\lambda = 600$ nm, i.e. a $\Delta\lambda = 97$ nm shift. However, for the symmetric case [25], considering gold bowtie nanoantennas (not shown), the blue-shift goes from $\lambda = 731$ nm to $\lambda = 566$ nm ($\Delta\lambda = 165$ nm) when changing $\theta'_1 = \theta'_2$ from 10° to 40°. Interestingly, a similar response is obtained for the orthogonal polarization (i.e. horizontal nanoemitter), shown in Figure 3F, with the localized surface plasmon of order $n = 1$ at the same location as the vertical polarization, $\lambda = 697$ nm for $\theta'_1 = 10°$ and $\lambda = 600$ nm for $\theta'_1 = 40°$. For symmetric bowtie nanoantennas, however, the fundamental localized surface plasmon mode is blue-shifted from $\lambda = 638$ nm to $\lambda = 517$ nm ($\Delta\lambda = 121$ nm) within the same range of $\theta'_1 = \theta'_2$. These results demonstrate that the overall $\overline{\Gamma_{nr}}$ spectra will be changed when introducing asymmetries into the nanoantennas, an aspect that is crucial in real-world scenarios where it is likely that fabrication errors and tolerances may produce asymmetric instead of symmetric bowtie nanoantennas.

Another noteworthy information is that the blue-shift of the $\overline{\Gamma_{nr}}$ spectra observed in Figure 3E and F result from

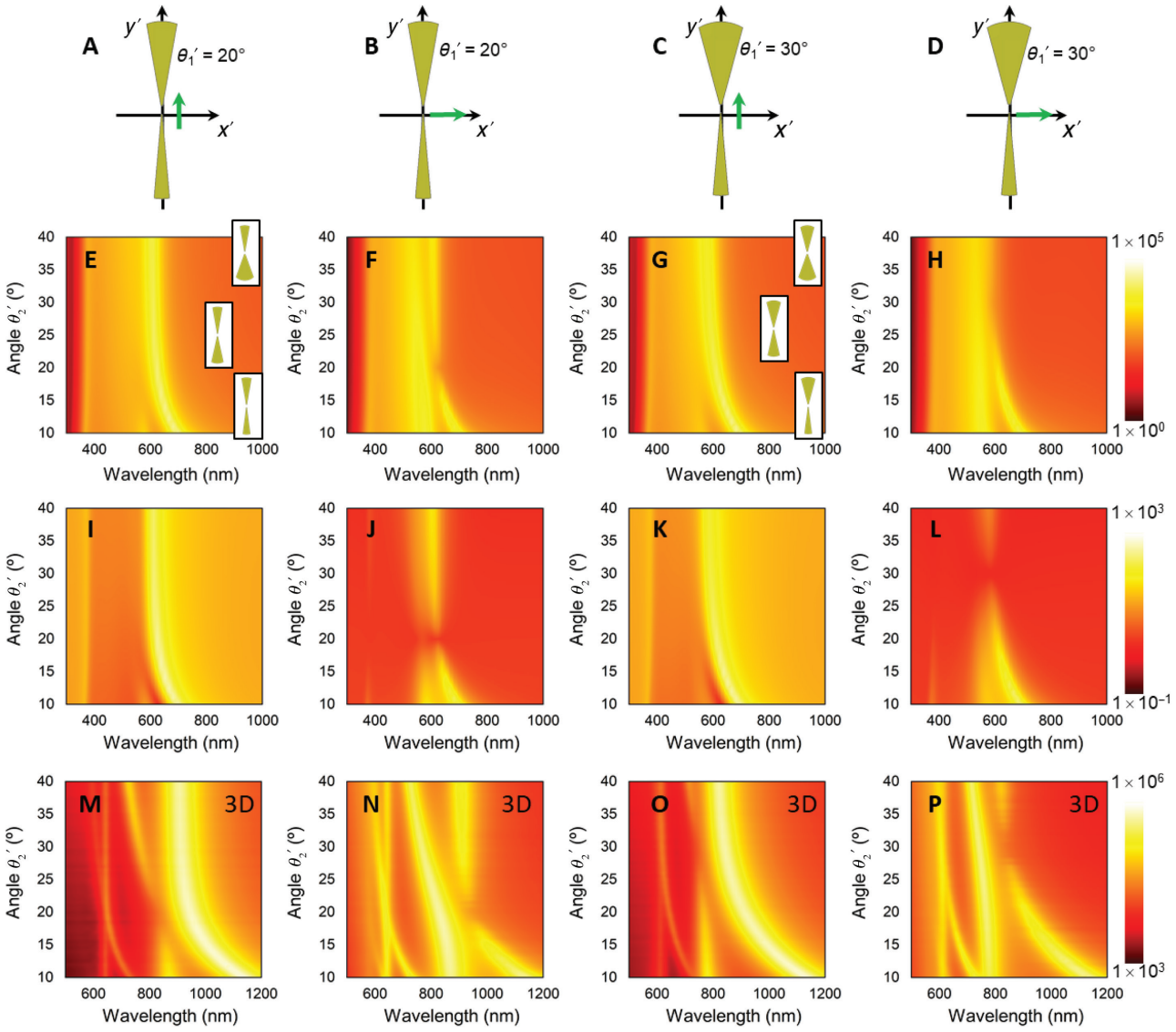

Figure 3: Non-radiative and radiative Purcell enhancement for asymmetric nanoantennas.
The schematic representation of the $l' = 20$ nm and $g' = 1$ nm bowtie nanoantenna with $\theta_1' = 20°$ (A, B) and $\theta_1' = 30°$ (C, D) illuminated by a vertical (A, C) and horizontal (B, D) nanoemitters; the nanoemitters are depicted by the green arrow. The corresponding $\overline{\Gamma_{nr}}$ (second row) and $\overline{\Gamma_r}$ (third row) 2D bowties, and simulated $\overline{\Gamma_{nr}}$ for a 1 nm-thick bowtie (bottom row). Insets in (E) and (G) depict the geometry of the bowtie for different θ_2'.

the hybridization between the spectrum produced by each of the arms of the bowtie nanoantennas (θ_1' and θ_2'). Hence, the arm with smaller θ' will dominate the spectrum. This can be corroborated by the results in Figure 4 where it is shown how for $\theta_2' < (\theta_1' = 20°)$, the shift of the localized surface plasmon modes is larger compared to the case when $\theta_2' > \theta_1'$. This is due to the fact that, in the former scenario, the $\overline{\Gamma_{nr}}$ spectrum is dominated by the arm with θ_2'. When $\theta_2' > \theta_1'$, the spectrum is dominated by the top arm with $\theta_1' = 20°$ and then the $\overline{\Gamma_{nr}}$ is saturated when increasing θ_2'. For the sake of completeness, the results of the radiated Purcell enhancement $\overline{\Gamma_r}$ spectra, which is calculated as the ratio between the power scattered by the bowtie nanoantenna and that radiated by the nanoemitter alone ($\overline{\Gamma_r} = P_r / P_0$), as a function of θ_2' are shown in Figure 3I and J for both vertical and horizontal nanoemitters, respectively. As observed, the $\overline{\Gamma_r}$ is almost two orders of magnitude lower than the $\overline{\Gamma_{nr}}$, thus confirming the assumption that radiation losses are negligible because $l' \ll \lambda_0$ (see Methods section for more details). We have also calculated the spectral response considering a different value of $\theta_1' = 30°$ and the results of the $\overline{\Gamma_{nr}}$ are shown in Figure 3G and H for the vertical and horizontal polarization of the nanoemitter, respectively, along with

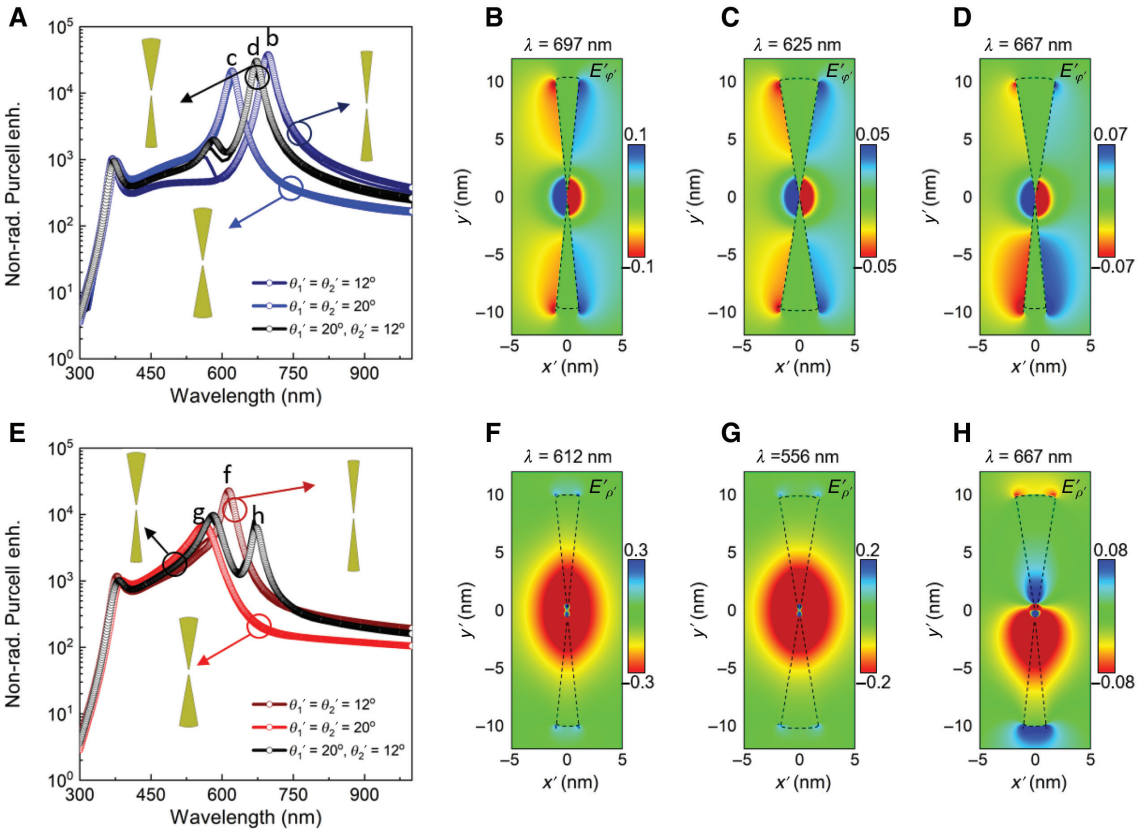

Figure 4: Comparison between symmetric and asymmetric bowtie nanoantennas.
The $\overline{\Gamma_{nr}}$ values for different sets of θ_1' and θ_2' corresponding to a vertical (A) and horizontal nanoemitter (E); the solid lines are the corresponding results obtained with COMSOL Multiphysics. Snapshot of the $E_{\varphi'}'$ field (B–D) and the $E_{\rho'}'$ field (F–H) at the fundamental peaks in (A) and (E), respectively, computed using COMSOL Multiphysics.

the results of the $\overline{\Gamma_r}$ for both polarizations (Figure 3K and L). Note that a similar performance as those previously discussed when considering $\theta_1' = 20°$ is obtained with this case where the localized surface plasmon modes are blue-shifted when changing θ_2' from 10° to 40°.

As we have shown in our previous works, the $\overline{\Gamma_{nr}}$ is determined by the coupling between the nanoemitters and the field profile of each localized surface plasmon mode supported by the bowtie nanoantennas [25]. As shown in Figure 3, the $\overline{\Gamma_{nr}}$ is increased when changing θ_2' to larger values, and this coupling can also be modified by changing the position of the nanoemitter along the x' or y' axis [13]. In this realm, there will either be a strong or low coupling of the radiated field from the nanoemitter to each LSP mode depending on its spatial location within the field distribution of each mode. This performance can also be observed in Figure 3, and it is more evident for the horizontal polarization of the nanoemitter (Figure 3F and H). The figures show how there is an LSP mode that is only excited when $\theta_2' \neq \theta_1'$, which is a result of the hybridization between the different modes excited in the asymmetric bowtie nanoantenna.

To further study this case, let us first consider the case of a vertical polarized nanoemitter illuminating an asymmetric bowtie nanoantenna with $\theta_1' = 20°$ and $\theta_2' = 12°$. The $\overline{\Gamma_{nr}}$ spectrum for this case, extracted from Figure 3E, is shown in Figure 4A as a black curve along with the $\overline{\Gamma_{nr}}$ spectra for symmetric bowtie nanoantennas with $\theta_1' = \theta_2' = 12°$ (dark blue) and $\theta_1' = \theta_2' = 20°$ (light blue). From these results, as expected, the peak of $\overline{\Gamma_{nr}}$ related to the LSP mode of order $n = 1$ for the asymmetric case lies in between those obtained using symmetric nanoantennas. For completeness, the field distribution for this LSP mode considering the two symmetric and asymmetric nanoantennas are shown in Figure 4B and C, respectively, which indicate how the same field distribution is obtained in all cases. For the orthogonal polarization, the results of the $\overline{\Gamma_{nr}}$ spectra are shown in Figure 4E considering the asymmetric and the two symmetric nanoantennas with angles of the arms as in Figure 4A. From these results, one can observe how the first peak of $\overline{\Gamma_{nr}}$ for the asymmetric case is no longer in between the two peaks of the symmetric nanoantennas and is now red-shifted. Moreover, note

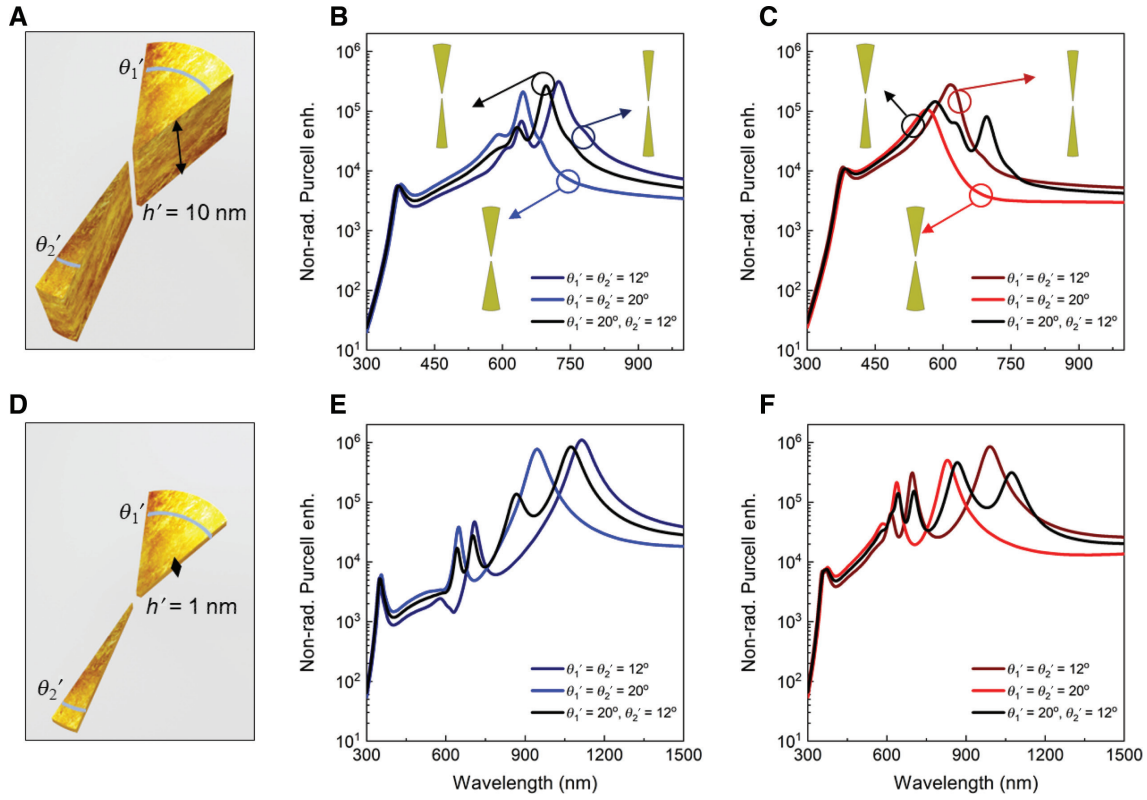

Figure 5: 3D asymmetric bowtie nanoantennas excited by a localized emitter.
The schematic representation of the 3D $l' = 20$ nm and $g' = 1$ nm bowties (A, D). The $\overline{\Gamma_{nr}}$ values for different sets of θ_1' and θ_2' corresponding to the vertical (second column) and horizontal nanoemitters (third column) for the 10-nm thick (top row) and 1-nm thick bowtie (bottom row).

that its field distribution is completely different (Figure 4H) to those of the symmetric nanoantennas (Figure 4F and G) due to the hybridization between the modes.

2.4 Three-dimensional nanoantennas

Conformal mapping enables us to provide an analytical solution only for 2D bowties (i.e. 3D bowties with infinite height). However, the physical insight gained can be transferred to realistic 3D bowties. We demonstrate this by using COMSOL Multiphysics to reproduce some of the previous results for 1-nm thick and 10-nm thick bowties with point dipoles at 0.5 nm and 5 nm height, respectively, modelling a 3D nanoemitter.

The bottom row in Figure 3 shows the $\overline{\Gamma_{nr}}$ for the 1-nm thick bowtie. These color maps show a more complex electromagnetic response than the 2D counterpart, but one can appreciate that the trends remain: the localized surface plasmon modes are blue-shifted when changing θ_2' and one can find a θ_2' such that $\overline{\Gamma_{nr}}$ vanishes. In fact, θ_2' is the same for the 2D and 3D cases.

The 1-nm thick bowtie is the most extreme case compared to the 2D scenario. Thicker bowties will not only retain the trends, but they will also have a similar spectra to the 2D scenario qualitatively and quantitatively in terms of wavelength. To demonstrate this, we refer the reader to compare Figure 5 with Figure 4A and E.

3 Methods

3.1 Analytical formulation

In this section, we show the analytical solution of the periodic metal-insulator geometry described in Figure 1B. As observed, this geometry is similar to the one shown in our previous work [25]. However, our aim here is to evaluate a more general case when $d_3 \neq d_4$ (i.e. the angles θ_1' and θ_2' of the two arms of the bowtie nanoantenna are different). To work within the quasi-static approximation, we assumed that bowtie nanoantennas are smaller than the wavelength of the illuminating source ($l' \ll \lambda_0$). In this realm, the electric and magnetic fields are decoupled and the former can be fully described by an electrostatic potential satisfying Laplace's equation. Moreover, since $L_1 + L_2 \gg \theta_1', \theta_2'$, the modes with phase variation along the y axis (longitudinal

modes) can be neglected. Hence, it can be assumed that the excited localized surface plasmon will be those with phase variation along the *x* axis (transversal modes). With these considerations, the potentials inside and outside the metals of the multislab geometry in Figure 1B can be defined as follows:

$$\sum_k \Upsilon[e^{ikx}+e^{-(kx-2ikL_1-i\Delta\varphi)}](C_+e^{-ky}+C_-e^{ky}),\quad -(d_1+2d_2+d_3+d_4)<y<-(d_1+2d_2+d_3) \tag{6}$$

$$\sum_k \Upsilon[e^{ikx}+e^{-(kx-2ikL_1-i\Delta\varphi)}](D_+e^{-ky}+D_-e^{ky}),\quad -(d_2+d_3)<y<-d_2 \tag{7}$$

$$\sum_k \Upsilon[e^{ikx}+e^{-(kx-2ikL_1-i\Delta\varphi)}](A_+e^{-ky}+B_+e^{-ky}+B_-e^{ky}),\quad 0<y<d_1 \tag{8}$$

$$\sum_k \Upsilon[e^{ikx}+e^{-(kx-2ikL_1-i\Delta\varphi)}](A_-e^{-ky}+B_+e^{-ky}+B_-e^{ky}),\quad -d_2<y<0 \tag{9}$$

$$\sum_k \Upsilon[e^{ikx}+e^{-(kx-2ikL_1-i\Delta\varphi)}](E_+e^{-ky}+E_-e^{ky}),\quad -(d_1+2d_2+d_3)<y<-(d_2+d_3) \tag{10}$$

where $\Upsilon=[1-e^{2ik(L_1+L_2+2i\Delta\varphi)}]^{-1}$, $k=(n\pi-\Delta\varphi)/(L_1+L_2)$ is the wave number of the localized surface plasmon modes with order $n=1, 2, 3\ldots$, $\Delta\varphi$ is the phase correction added to the system to consider the nonperfect reflections at the end faces of the periodic metal-insulator cavities, and (B_+, B_-) and (E_+, E_-) are the constants corresponding to the potential in those regions where the nanoemitter is present or absent, respectively. In addition, (C_+, C_-) and (D_+, D_-) are the constants inside the metal strips d_4 and d_3, respectively. Finally, the coefficients for the incident potential (A_+, A_-) can be calculated by expanding the potential of the dipole nanoemitter using a Fourier transform along the *x* axis as $A_\pm=(\pm p_y-ip_x\mathrm{sgn}(k))/(2\varepsilon_0)$, with $p_{x,y}$ as the components of the dipole moment along the *x* and *y* axis, respectively, and ε_0 as the permittivity in free space. The other coefficients ($B_\pm$, $C_\pm$, $D_\pm$ and $E_\pm$) can be calculated by simply introducing two boundary conditions: the continuity of the parallel component of the electric field (E_x) along with the conservation of the perpendicular component of the displacement current ($D_y=\varepsilon_{Au}E_y$) at the boundaries d_1, d_2, d_2+d_3 and $d_1+2d_2+d_3+d_4$:

$$A_+e^{-kd_1}+B_+e^{-kd_1}+B_-e^{kd_1}=C_+e^{k(d_1+2d_2+d_3+d_4)}+C_-e^{-k(d_1+2d_2+d_3+d_4)} \tag{11}$$

$$A_+e^{-kd_1}+B_+e^{-kd_1}-B_-e^{kd_1}=\varepsilon_{Au}C_+e^{k(d_1+2d_2+d_3+d_4)}-\varepsilon_{Au}C_-e^{-k(d_1+2d_2+d_3+d_4)} \tag{12}$$

$$A_-e^{-kd_2}+B_+e^{kd_2}+B_-e^{-kd_2}=D_+e^{kd_2}+D_-e^{-kd_2} \tag{13}$$

$$A_-e^{-kd_2}-B_+e^{kd_2}+B_-e^{-kd_2}=-\varepsilon_{Au}D_+e^{kd_2}+\varepsilon_{Au}D_-e^{-kd_2} \tag{14}$$

$$E_+e^{k(d_2+d_3)}+E_-e^{-k(d_2+d_3)}=D_+e^{k(d_2+d_3)}+D_-e^{-k(d_2+d_3)} \tag{15}$$

$$E_+e^{k(d_2+d_3)}-E_-e^{-k(d_2+d_3)}=\varepsilon_{Au}D_+e^{k(d_2+d_3)}-\varepsilon_{Au}D_-e^{-k(d_2+d_3)} \tag{16}$$

$$E_+e^{k(d_1+2d_2+d_3)}+E_-e^{-k(d_1+2d_2+d_3)}=C_+e^{k(d_1+2d_2+d_3)}+C_-e^{-k(d_1+2d_2+d_3)} \tag{17}$$

$$-E_+e^{k(d_1+2d_2+d_3)}+E_-e^{-k(d_1+2d_2+d_3)}=-\varepsilon_{Au}C_+e^{k(d_1+2d_2+d_3)}+\varepsilon_{Au}C_-e^{-k(d_1+2d_2+d_3)} \tag{18}$$

with ε_{Au} as the permittivity of the metal used in this work for the bowtie nanoantennas (gold). As in our previous works, the solutions of these equations can be calculated straightforwardly either manually or via a mathematical software. For the sake of brevity, however, we will not show the whole expressions for the constants in this paper. After applying an inverse transform to the induced potentials, the solutions for the potentials where the dipole is present (Φ_1^s) and absent (Φ_2^s) as well as inside the metal slabs, (Φ_1^m) and (Φ_2^m), are as follows:

$$\Phi_1^s=\Omega\sum_n\{p_x[\sin(kx)-\sin(kx-2kL_1-\Delta\varphi)]+p_y[\cos(kx)+\cos(kx-2kL_1-\Delta\varphi)]\}(B_+e^{-ky}+B_-e^{ky}) \tag{19}$$

$$\Phi_2^s=\Omega\sum_n\{p_x[\sin(kx)-\sin(kx-2kL_1-\Delta\varphi)]+p_y[\cos(kx)+\cos(kx-2kL_1-\Delta\varphi)]\}(E_+e^{-ky}+E_-e^{ky}) \tag{20}$$

$$\Phi_1^m=\Omega\sum_n\{p_x[\sin(kx)-\sin(kx-2kL_1-\Delta\varphi)]+p_y[\cos(kx)+\cos(kx-2kL_1-\Delta\varphi)]\}(C_+e^{-ky}+C_-e^{ky}) \tag{21}$$

$$\Phi_2^m=\Omega\sum_n\{p_x[\sin(kx)-\sin(kx-2kL_1-\Delta\varphi)]+p_y[\cos(kx)+\cos(kx-2kL_1-\Delta\varphi)]\}(D_+e^{-ky}+D_-e^{ky}) \tag{22}$$

with $\Omega=[2\varepsilon_0(L_1+L_2)]^{-1/2}$. Once the potentials are calculated, the final step consists of simply differentiating these expressions to calculate the *x* and *y* components of

the electric field in each region of periodic metal-insulator geometry:

$$E_{1x}^{s} = -k\Omega\sum_{n}\{p_x[\cos(kx)-\cos(kx-2kL_1-\Delta\varphi)] - p_y[\sin(kx)+\sin(kx-2kL_1-\Delta\varphi)]\}(B_{+}e^{-ky}+B_{-}e^{ky}) \quad (23)$$

$$E_{2x}^{s} = -k\Omega\sum_{n}\{p_x[\cos(kx)-\cos(kx-2kL_1-\Delta\varphi)] - p_y[\sin(kx)+\sin(kx-2kL_1-\Delta\varphi)]\}(E_{+}e^{-ky}+E_{-}e^{ky}) \quad (24)$$

$$E_{1x}^{m} = -k\Omega\sum_{n}\{p_x[\cos(kx)-\cos(kx-2kL_1-\Delta\varphi)] - p_y[\sin(kx)+\sin(kx-2kL_1-\Delta\varphi)]\}(C_{+}e^{-ky}+C_{-}e^{ky}) \quad (25)$$

$$E_{2x}^{m} = -k\Omega\sum_{n}\{p_x[\cos(kx)-\cos(kx-2kL_1-\Delta\varphi)] - p_y[\sin(kx)+\sin(kx-2kL_1-\Delta\varphi)]\}(D_{+}e^{-ky}+D_{-}e^{ky}) \quad (26)$$

$$E_{1y}^{s} = -k\Omega\sum_{n}\{p_x[\sin(kx)-\sin(kx-2kL_1-\Delta\varphi)] - p_y[\cos(kx)+\cos(kx-2kL_1-\Delta\varphi)]\}(-B_{+}e^{-ky}+B_{-}e^{ky}) \quad (27)$$

$$E_{2y}^{s} = -k\Omega\sum_{n}\{p_x[\sin(kx)-\sin(kx-2kL_1-\Delta\varphi)] - p_y[\cos(kx)+\cos(kx-2kL_1-\Delta\varphi)]\}(-E_{+}e^{-ky}+E_{-}e^{ky}) \quad (28)$$

$$E_{1y}^{m} = -k\Omega\sum_{n}\{p_x[\sin(kx)-\sin(kx-2kL_1-\Delta\varphi)] - p_y[\cos(kx)+\cos(kx-2kL_1-\Delta\varphi)]\}(-C_{+}e^{-ky}+C_{-}e^{ky}) \quad (29)$$

$$E_{2y}^{m} = -k\Omega\sum_{n}\{p_x[\sin(kx)-\sin(kx-2kL_1-\Delta\varphi)] - p_y[\cos(kx)+\cos(kx-2kL_1-\Delta\varphi)]\}(-D_{+}e^{-ky}+D_{-}e^{ky}) \quad (30)$$

3.2 Numerical simulations

All simulations in this manuscript were carried out using the frequency domain solver of the commercial software COMSOL Multiphysics following the same setup as in our previous studies [25–27]. Gold permittivity was modeled using an analytical polynomial equation. This function fits Palik's experimental data [55]. The bowties were immersed within a box of 600 nm side filled with vacuum. Scattering boundary conditions were applied around this box to avoid undesirable reflections. The nanoemitter was modeled using two anti-parallel, in-plane magnetic currents with a distance of 5 pm between them. A refined mesh with a minimum and maximum size of 3 pm and 2 nm was implemented for the vacuum box to ensure accurate results. The mesh used for the bowtie nanoantennas was refined to be two times smaller than that of the 600-nm box.

4 Conclusions and remarks

The analytical solutions for plasmonics nanoantennas are scarce. Conformal mapping is well-positioned to address the challenge because of its simplicity and ability to produce closed-form formulas. Here, the contributions of different groups to conformal mapping nanoantennas have been reviewed briefly. The study also presented how conformal mapping provides an easy solution to study in particular bowtie nanoantennas, even those with some degree of asymmetry, which in a real-life application, could have been induced intentionally to favor Fano line shapes for spectroscopy or unintentionally due to nanofabrication limitations. Although conformal mapping deals with 2D scenarios, its results provide a qualitative knowledge about the spatial and wavelength dependence of the electromagnetic response of the 3D fabricated nanoantennas.

Acknowledgment: VPP is supported by the Newcastle University (Newcastle University Research Fellow, Funder Id: http://dx.doi.org/10.13039/501100000774). RA is supported by the University of Birmingham (Ph.D. studentship). MNC is supported by the University of Birmingham (Birmingham Fellowship, Funder Id: http://dx.doi.org/10.13039/501100000855) and the EPSRC (Grant No. EP/S018395/1, Funder Id: http://dx.doi.org/10.13039/501100000266).

References

[1] Maier SA. Plasmonics: fundamentals and applications. US, Springer, 2007, 1–223. ISBN: 9780387331508.
[2] Kinkhabwala A, Yu Z, Fan S, Avlasevich Y, Müllen K, Moerner WE. Large single-molecule fluorescence enhancements produced by a bowtie nanoantenna. Nat Photon 2009;3:654–7.
[3] Chikkaraddy R, de Nijs B, Benz F, et al. Single-molecule strong coupling at room temperature in plasmonic nanocavities. Nature 2016;535:127–30.
[4] Aouani H, Rahmani M, Navarro-Cía M, Maier SA. Third-harmonic-upconversion enhancement from a single semi-conductor nanoparticle coupled to a plasmonic antenna. Nat Nanotechnol 2014;9:290–4.

[5] Lee J, Nookala N, Gomez-Diaz JS, et al. Ultrathin second-harmonic metasurfaces with record-high nonlinear optical response. Adv Opt Mater 2016;4:664–70.
[6] Benz F, Schmidt MK, Dreismann A, et al. Single-molecule optomechanics in "picocavities". Science 2016;354:726–9.
[7] Lundeberg MB, Gao Y, Asgari R, et al. Tuning quantum nonlocal effects in graphene plasmonics. Science 2017;357:187–91.
[8] Eggleston MS, Messer K, Zhang L, Yablonovitch E, Wu MC. Optical antenna enhanced spontaneous emission. Proc Natl Acad Sci USA 2015;112:1704–9.
[9] Ayata M, Fedoryshyn Y, Heni W, et al. High-speed plasmonic modulator in a single metal layer. Science 2017;11:630–2.
[10] Haffner C, Chelladurai D, Fedoryshyn Y, et al. Low-loss plasmon-assisted electro-optic modulator. Nature 2018;556:483–6.
[11] Kraft M, Pendry JB, Maier SA, Luo Y. Transformation optics and hidden symmetries. Phys Rev B 2014;89:1–10.
[12] Huidobro PA, Chang YH, Kraft M, Pendry JB. Hidden symmetries in plasmonic gratings. Phys Rev B 2017;95:1–8.
[13] Pacheco-Peña V, Alves R, Navarro-Cía M. Hidden symmetries in bowtie nanocavities and diabolo nanoantennas. ACS Photon 2019;6:2014–24.
[14] Li R, Bowerman B. Symmetry breaking in biology. Cold Spring Harbor Perspect Biol 2010;2:1521–8.
[15] Cetin AE, Altug H. Fano resonant ring/disk plasmonic nanocavities on conducting substrates for advanced biosensing. ACS Nano 2012;6:9989–95.
[16] Butet J, Thyagarajan K, Martin OJF. Ultrasensitive optical shape characterization of gold nanoantennas using second harmonic generation. Nano Lett 2013;13:1787–92.
[17] Cao T, Bao J, Mao L, et al. Controlling lateral fano interference optical force with Au-Ge2Sb2Te5 hybrid nanostructure. ACS Photon 2016;3:1934–42.
[18] Kadic M, Guenneau S, Enoch S, et al. Transformation plasmonics. Nanophotonics 2012;1:51–64.
[19] Zhang J, Pendry JB, Luo Y. Transformation optics from macroscopic to nanoscale regimes: a review. Adv Photon 2019;1:1.
[20] Xu L, Chen HY. Conformal transformation optics. Nat Photon 2014;9:15–23.
[21] Navarro-Cia M, Maier SA. Broad-band near-infrared plasmonic nanoantennas for higher harmonic generation. ACS Nano 2012;6:3537–44.
[22] Aouani H, Navarro-Cia M, Rahmani M, et al. Multiresonant broadband optical antennas as efficient tunable nanosources of second harmonic light. Nano Lett 2012;12:4997–5002.
[23] Aouani H, Rahmani M, Šípová H, et al. Plasmonic nanoantennas for multispectral surface-enhanced spectroscopies. J Phys Chem C 2013;117:18620–6.
[24] Aouani H, Šípová H, Rahmani M, et al. Ultrasensitive broadband probing of molecular vibrational modes with multifrequency optical antennas. ACS Nano 2013;7:669–75.
[25] Pacheco-Peña V, Beruete M, Fernández-Domínguez AI, Luo Y, Navarro-Cía M. Description of bow-tie nanoantennas excited by localized emitters using conformal transformation. ACS Photon 2016;3:1223–32.
[26] Pacheco-Peña V, Fernández-Domínguez AI, Luo Y, Beruete M, Navarro-Cía M. Aluminum nanotripods for light-matter coupling robust to nanoemitter orientation. Laser Photon Rev 2017;11:1–6.
[27] Pacheco-Peña V, Navarro-Cía M. Understanding quantum emitters in plasmonic nanocavities with conformal transformation: Purcell enhancement and forces. Nanoscale 2018;10:13607–16.
[28] Burington RS. On the use of conformal mapping in shaping wing profiles. Am Math Month 1940;47:362–73.
[29] Garg R, Bahl I, Bozzi M. Microstrip lines and slotlines. 3rd, Boston, USA. Artech House, 2013, 560. ISBN: 9781608075355.
[30] Aubry A, Lei DY, Fernández-Domínguez AI, Sonnefraud Y, Maier SA, Pendry JB. Plasmonic light-harvesting devices over the whole visible spectrum. Nano Lett 2010;10:2574–9.
[31] Lei DY, Aubry A, Maier SA, Pendry JB. Broadband nanofocusing of light using kissing nanowires. N J Phys 2010;12:093030.
[32] Lei DY, Aubry A, Luo Y, Maier SA, Pendry JB. Plasmonic interaction between overlapping nanowires. ACS Nano 2011;5:597–607.
[33] Luo Y, Pendry JB, Aubry A. Surface plasmons and singularities. Nano Lett 2010;10:4186–91.
[34] Luo Y, Aubry A, Pendry JB. Electromagnetic contribution to surface-enhanced Raman scattering from rough metal surfaces: a transformation optics approach. Phys Rev B 2011;83:1–11.
[35] Galiffi E, Pendry JB, Huidobro PA. Broadband tunable THz absorption with singular graphene metasurfaces. ACS Nano 2018;12:1006–13.
[36] Zeng Y, Liu J, Werner DH. General properties of two-dimensional conformal transformations in electrostatics. Opt Express 2011;19:20035.
[37] Zhang J, Zayats A. Multiple Fano resonances in single-layer non-concentric core-shell nanostructures. Opt Express 2013;21:8426.
[38] Zhang J, Wubs M, Ginzburg P, Wurtz G, Zayats AV. Transformation quantum optics: designing spontaneous emission using coordinate transformations. J Opt 2016;18:044029.
[39] Fernández-Domínguez AI, Wiener A, García-Vidal FJ, Maier SA, Pendry JB. Transformation-optics description of nonlocal effects in plasmonic nanostructures. Phys Rev Lett 2012;108:1–5.
[40] Hanham SM, Fernández-Domínguez AI, Teng JH, et al. Broadband terahertz plasmonic response of touching InSb disks. Adv Mater 2012;24:226–30.
[41] Demetriadou A, Hamm JM, Luo Y, Pendry JB, Baumberg JJ, Hess O. Spatiotemporal dynamics and control of strong coupling in plasmonic nanocavities. ACS Photon 2017;4:2410–8.
[42] Fernández-Domínguez AI, Maier SA, Pendry JB. Collection and concentration of light by touching spheres: a transformation optics approach. Phys Rev Lett 2010;105:2–5.
[43] Li RQ, Hernángomez-Pérez D, García-Vidal FJ, Fernández-Domínguez AI. Transformation optics approach to plasmon-exciton strong coupling in nanocavities. Phys Rev Lett 2016;117:1–5.
[44] Aubry A, Lei DY, Maier SA, Pendry JB. Broadband plasmonic device concentrating the energy at the nanoscale: the crescent-shaped cylinder. Phys Rev B 2010;82:1–9.
[45] Fernández-Domínguez AI, Luo Y, Wiener A, Pendry JB, Maier SA. Theory of three-dimensional nanocrescent light harvesters. Nano Lett 2012;12:5946–53.
[46] Wang L, Uppuluri SM, Jin EX, Xu X. Nanolithography using high transmission nanoscale bowtie apertures. Nano Lett 2006;6:361–4.
[47] Mivelle M, van Zanten TS, Neumann L, van Hulst NF, Garcia-Parajo MF. Ultrabright bowtie nanoaperture antenna

probes studied by single molecule fluorescence. Nano Lett 2012;12:5972–8.
[48] Roxworthy BJ, Ko KD, Kumar A, et al. Application of plasmonic bowtie nanoantenna arrays for optical trapping, stacking, and sorting. Nano Lett 2012;12:796–801.
[49] Santhosh K, Bitton O, Chuntonov L, Haran G. Vacuum Rabi splitting in a plasmonic cavity at the single quantum emitter limit. Nat Commun 2016;7:1–5.
[50] Giannini V, Fernández-Domínguez AI, Sonnefraud Y, Roschuk T, Fernández-García R, Maier SA. Controlling light localization and light-matter interactions with nanoplasmonics. Small 2010;6:2498–507.
[51] Chandran A, Barnard ES, White JS, Brongersma ML. Metal-dielectric-metal surface plasmon-polariton resonators. Phys Rev B 2012;85:1–9.
[52] Yang F, Huidobro PA, Pendry JB. Transformation optics approach to singular metasurfaces. Phys Rev B 2018;98:1–20.
[53] Felsen LB, Marcuvitz N. Radiation and scattering of waves. Hoboken, NJ, USA, Wiley-IEEE Press, 2001:1–924.
[54] Ishimaru A. Electromagnetic wave propagation, radiation, and scattering. Hoboken, NJ, USA, John Wiley & Sons, Inc., 2017:1–940.
[55] Palik ED, editor. Handbook of optical constants of solids. San Diego, USA, Elsevier, 1985.